Journal of Catalysis 361 (2018) 414–422

Contents lists available at ScienceDirect

Journal of Catalysis

journal homepage: www.elsevier.com/locate/jcat

Mechanistic understanding of methanol carbonylation: Interfacing homogeneous and heterogeneous catalysis via carbon supported Ir—La

Alyssa J.R. Hensley [a], Jianghao Zhang [a], Ilka Vinçon [b], Xavier Pereira Hernandez [a], Diana Tranca [b], Gotthard Seifert [b,*], Jean-Sabin McEwen [a,c,d,e,*], Yong Wang [a,e,*]

[a] The Gene and Linda Voiland School of Chemical Engineering and Bioengineering, Washington State University, Pullman, WA 99164, United States
[b] Theoretical Chemistry, Technische Universität Dresden, Dresden 01062, Germany
[c] Department of Physics and Astronomy, Washington State University, Pullman, WA 99164, United States
[d] Department of Chemistry, Washington State University, Pullman, WA 99164, United States
[e] Institute for Integrated Catalysis, Pacific Northwest National Laboratory, Richland, WA 99352, United States

ARTICLE INFO

Article history:
Received 17 July 2017
Revised 21 February 2018
Accepted 22 February 2018
Available online 5 April 2018

Keywords:
Single-site heterogeneous catalyst
Methanol carbonylation
Ir—La complex
Promoter effects
Density functional theory
Attenuated total reflectance-Fourier transform infrared spectroscopy

ABSTRACT

The creation of heterogeneous analogs to homogeneous catalysts is of great importance to many industrial processes. Acetic acid synthesis via the carbonylation of methanol is one such process and it relies on a difficult-to-separate homogeneous Ir-based catalyst. Using a combination of density functional theory (DFT) and attenuated total reflectance-Fourier transform infrared (ATR-FTIR) spectroscopy, we determine the structure and mechanism for methanol carbonylation over a promising single-site Ir—La/C heterogeneous catalyst replacement. Here, the Ir center is the active site with the acetyl-Ir complex being a rate controlling intermediate. Furthermore, the La both atomically disperses the Ir and acts as a Lewis acid site. In fact, the La promoter in the Ir—La/C catalyst was found to behave similarly to homogeneous promoters by abstracting an iodine from the Ir center and accelerating the CO insertion step. Overall, this work provides key insight into the atomistic nature of the Ir—La/C single-site catalyst and allows for the further design and optimization of single-site heterogeneous catalysts.

© 2018 Elsevier Inc. All rights reserved.

1. Introduction

Single-site heterogeneous catalysts are a new class of materials that interface the heterogeneous and homogeneous paradigms, combining the high activity and selectivity of homogeneous catalysts with the high separability of heterogeneous catalysts. Examples of such catalysts include bimetallic surfaces with an atomically dispersed noble metal supported on a base metal or oxide surface, as well as being exchanged into zeolites [1–9]. One industrially homogeneous catalytic process currently without a viable heterogeneous replacement [10–12] is the production of acetic acid which is accomplished via the carbonylation of methanol through either the Monsanto process with an Rh catalyst [10,13,14] or the Cativa process with an Ir catalyst with a Ru promoter [14–18]. The mechanism for the catalysis has the same major steps for both processes [14,15], with the key steps being the oxidative addition of iodomethane (MeI) to the reduced metal center ($[M(CO)_2I_2]^-$) and the migratory insertion of CO into the methyl-metal bond followed by the reductive elimination of acetyl iodide (AcI) as the product [10,19–21]. In our recent work, we reported a promising heterogeneous catalyst for the carbonylation of methanol based on Ir and a La promoter [11]. Characterization of this Ir—La/C system showed that the catalyst was a molecular species with distinct sites formed from two metal atoms [11], essentially creating a single-site catalyst on an activated carbon support. Overall, the heterogeneous Ir—La/C catalyst showed comparable reactivity and selectivity to the analogous homogeneous catalyst [11]. Furthermore, using La as a promoter as opposed to Ru can also reduce the cost of the catalyst. Thus, the Ir—La/C heterogeneous catalyst is a promising alternative to the conventional homogeneous system for the carbonylation of methanol to acetic acid.

Here, we establish the structure and methanol carbonylation mechanism of the heterogeneous Ir—La/C catalyst using a combination of density functional theory (DFT) and attenuated total reflectance-Fourier transform infrared (ATR-FTIR) spectroscopy. Additionally, we have elucidated the role of the La promoter in the carbonylation reaction. Overall, this work shows that the

* Corresponding authors at: The Gene and Linda Voiland School of Chemical Engineering and Bioengineering, Washington State University, Pullman, WA 99164, United States (J.-S. McEwen and Y. Wang).
E-mail addresses: gotthard.seifert@chemie.tu-dresden.de (G. Seifert), js.mcewen@wsu.edu (J.-S. McEwen), yong.wang@pnnl.gov (Y. Wang).

https://doi.org/10.1016/j.jcat.2018.02.022
0021-9517/© 2018 Elsevier Inc. All rights reserved.

dispersion and activity of single-site heterogeneous catalysts can be tuned via the choice of promoter (i.e. altering the promoter's oxygen affinity and electronegativity/Lewis acidity), thereby allowing for the greater design and optimization of heterogeneous catalysts for the carbonylation of methanol.

2. Methods and materials

2.1. Density functional theory

DFT calculations were carried out using the Vienna *Ab Initio* Simulation Package (VASP) [22–24]. The projector-augmented wave (PAW) method [25,26] with a plane-wave basis set and an energy cutoff of 450 eV were used. To model the electron exchange and correlation, the Perdew-Burke-Ernzerhof (PBE) functional [27] has been applied. Spin polarization has been included in all calculations. The Gaussian smearing [28] method was used with a smearing width of 0.2 eV to improve convergence, and the total energy was extrapolated to zero Kelvin. All gas phase ground state optimizations used the conjugate gradient method and were considered converged when the interatomic forces were smaller than 0.01 eV/Å, while surface relaxations were considered converged when the forces were less than 0.025 eV/Å. The energy tolerance was set to 10^{-7} eV. Calculations for molecules in the gas phase were performed using an $18 \times 19 \times 20$ Å box, and one single **k**-point, the Gamma point, was sufficient to span the Brillouin zone. *Ab Initio* Molecular Dynamics (AIMD) simulations have been computed for a NVT ensemble at 513 K, which is the reaction temperature. As the spin-polarized ground state optimizations resulted in a net zero magnetic moment for the complexes examined here, the AIMD calculations were not spin polarized and the energy tolerance was set to 10^{-5} eV. The transition states calculated here were obtained using the Climbing Image Nudged Elastic Band (CINEB) method [29]. The optimizations along the minimum energy pathways (MEPs) were performed with the fast inertial relaxation engine (FIRE) optimizer with force and energy tolerances of 0.05 eV/Å and 10^{-7} eV, respectively [30,31]. Each transition state was found to have one imaginary vibrational mode along a given reaction pathway [32].

In order to make a stronger connection between the theory and experiment in this work, we calculated the Gibbs energy for our tested methanol carbonylation reaction pathways using standard statistical mechanics principles [33]. The Gibbs energy for each configuration was calculated as:

$$G_i = E_i - k_B T ln(q_{trans} q_{rot} q_{vib}) \tag{1}$$

where E_i is the DFT-calculated energy for the ith configuration; q_{trans}, q_{rot}, and q_{vib} are the translation, rotational, and vibrational partition functions; and k_B and T are Boltzmann's constant and the reaction temperature, respectively. In this study, the gas phase Ir—La complexes were treated as the model surface in each case, and therefore only the vibrational entropy associated with each complex was included in the Gibbs energies. However, the translational, rotational, and vibrational entropy contributions from the gas phase CO, MeI, and AcI species were included for the relevant ground state configurations. The partition functions were calculated according to [34]:

$$q_{trans} = \frac{(2\pi m k_B T)^{3/2}}{h^3} * \frac{k_B T}{P} \tag{2}$$

$$q_{rot,linear} = \frac{8\pi^2 I_{linear} k_B T}{h^2} \tag{3}$$

$$q_{rot,non-linear} = \frac{8\pi^2 (2\pi k_B T)^{3/2} \sqrt{I_A I_B I_C}}{\sigma h^3} \tag{4}$$

$$q_{vib} = \prod_i \frac{e^{-h\upsilon_i/2k_B T}}{1 - e^{-h\upsilon_i/k_B T}} \tag{5}$$

where m and P are the mass and partial pressure of the molecule of interest; I_{linear} is the moment of inertia for a linear molecule; I_A, I_B, and I_C are the principal moments of inertia of the molecule of interest (non-linear case); σ is the symmetry number for the molecule of interest; and υ_i is the ith vibrational mode. All Gibbs energies were calculated at a temperature of 513 K, a total pressure of 17 bar, a CO concentration of 17.3 mol%, a MeI concentration of 1.8 mol%, and an AcI concentration of 1.8 mol%, consistent with the catalytic experiments performed in our previous work (see Supplementary Material for more details) [11].

For the surface calculations, a single layer carbon sheet was simulated to represent the activated carbon support. The single layer sheet was found to be sufficient as only weak interactions exist between different layers of graphite and the influence of multiple graphene layers on adsorption energies is negligible [35]. Two different adsorption sites have been modeled using VASP and are shown in Fig. S1; a pristine graphene sheet to represent the basal planes and an OH-passivated armchair-graphene nanoribon (AGNR-OH) to simulate an adsorption edge (Fig. S1). An optimized lattice constant of 2.467 Å was found for graphene which is consistent with previous theoretical results [36,37]. The **k**-point mesh was optimized and a $(3 \times 3 \times 1)$ Monkhorst-Pack mesh [38] for the pristine graphene has been used. A vacuum slab of 20 Å was found to be sufficient to separate the layers. To simulate the graphene sheet, a p(6×6) supercell was used, which consisted of 72 atoms in the surface layer. These input parameters were necessary in order to minimize the lateral interactions between adjacent metal complexes. A $(1 \times 2 \times 3)$ Monkhorst-Pack mesh was applied for the p(5×9) supercell used to model the AGNR-OH surface. The edge-to-edge and layer-to-layer distance between AGNR-OH in the supercell is 13 Å and 17 Å, respectively. Binding energies for the adsorption of the Ir—La complex were calculated as:

$$E_b = E_{IrLa/C} - E_C - E_{IrLa} \tag{6}$$

where $E_{IrLa/C}$, E_C, and E_{IrLa} are the total energies of the adsorbed Ir—La complex, the respective surface site, and the Ir—La complex in the gas phase.

Density functional perturbation theory (DFPT) was used to generate the theoretical IR spectra presented here [39]. From DFPT, the Born effective charges and vibrational modes for our structures of interest were calculated and then used to obtained discrete IR intensities for each vibrational mode via a code provided by Karhánek et al., see Fig. S2 [40,41]. We then generated spectra for each vibrational mode by applying a Lorentzian distribution to each discrete point according to:

$$L(\nu) = \frac{1}{2\pi} \frac{w}{(\nu - \nu_0)^2 + \left(\frac{1}{2}w\right)^2} \tag{7}$$

where w and ν are the peak width and wavenumber, respectively. Each distribution is centered around ν_0, which is the vibrational mode of interest, and normalized such that the maximum value of L(ν) is equal to the calculated IR intensity. Finally, the spectra of the individual vibrational modes calculated for a single structure are summed in order to generate the overall vibrational spectra for each structure of interest (Fig. S2). All theoretical spectra shown here used a peak width of 35 cm^{-1}. Using the method presented here, we calculated the CO stretch frequencies for model

active centers in Fe hydrogenases (Table S1) and a comparison to experimental spectra showed that our calculated frequencies were accurate to within 5 cm^{-1} (see Table S1 for details) [42–44].

2.2. Catalyst preparation

The 5 wt% Ir/C and 5 wt% Ir—La/C (molar ratio of Ir to La = 1:1) catalysts were prepared by incipient wetness impregnation, where 5 wt% was chosen to improve the signal to noise ratio in the ATR-FTIR measurement. To prepare the 5 wt% Ir—La/C catalyst, a set amount (corresponding to Ir/catalyst weight ratio as 5 wt%) of $IrCl_3{\cdot}H_2O$ (American Elements, 56.4%Ir) and $LaCl_3{\cdot}7H_2O$ (Sigma-Aldrich, 99.999%) was dissolved in a particular amount of Milli-Q water. The amount of water corresponded to the pore volume of the carbon support (TA60, PICATAL). The as-prepared solution was added drop-wise to the support. Then, the support/solution mixture was manually stirred with a glass rod for approximately 20 min in order to ensure an even dispersion of solution over the support surface. The samples were then dried at 353 K overnight and calcined with continuous flow of N_2 at 573 K for 1 h. The 5 wt% Ir/C catalyst was prepared with the same procedure except that no $LaCl_3{\cdot}7H_2O$ was dissolved in the solution. These samples are expected to be atomically dispersed as they have two (symmetric and asymmetric) CO vibration peaks (Fig. 2a) after syngas pretreatment to the catalysts, which is the typical indication of single Ir atom species. Additionally, the intensity of the CO peaks for 5 wt % catalysts after syngas pretreatment is about 5 times of the 1 wt% catalysts (not shown) which were demonstrated to reach atomic dispersion [11].

2.3. Characterization

ATR-FTIR spectroscopy was employed to obtain information about the surface of the catalysts during the reaction and how the two metals (Ir and La) are anchored to the carbon support. The measurements were performed using a Bruker Tensor II spectrometer and a custom-made ATR-FTIR cell with a configuration previously reported [45]. ATR-FTIR was chosen because the evanescent wave during the total reflectance of the IR beam penetrates the surface of the sample by only a few micrometers which mitigates the loss of signal due to absorbance in the IR region by the carbon support [46].

The ATR-FTIR experiments were performed by depositing a catalyst coating layer on top of a ZnSe Internal Reflection Element (IRE). The sample coating was prepared by first grinding the as-prepared catalysts with a ball mill into very fine powders, which were subsequently suspended in Milli-Q water (1.5 mg catalyst/mL water). The suspension was then sonicated for approximately 1 min to form an ink and deposited on the ZnSe IRE. The ink covered IRE was dried at 363 K for 1 h to remove water, thereby creating a catalyst coating on the IRE.

For each ATR-FTIR experiment, the catalyst coated IRE was first calcined in N_2 (40 mL/min) at 553 K for 20 min. Then, the temperature of the cell was reduced to 513 K followed by flowing syngas (40 mL/min, CO/H_2 = 4/1), methanol (5.0 vol%, bubbled by syngas at 293 K), and MeI (1.5 vol% bubbled by syngas at 273 K). The total pressure for the reactions was set as 3.75 bar. During the reaction, spectra were recorded between 800 cm^{-1} and 4000 cm^{-1} by averaging 128 scans at a resolution of 4 cm^{-1} to improve the signal to noise ratio.

To determine how the Ir and La are anchored on the carbon surface, the spectra of the clean IRE was taken as a background. After the catalyst or pure carbon support was coated on the ZnSe crystal, the samples were pretreated with N_2 at 553 K and syngas at 513 K for 20 min successively. The spectra were then taken between 800 cm^{-1} and 4000 cm^{-1} by averaging 128 scans at a resolution of 4 cm^{-1}. Peak deconvolution was conducted by the PeakFit v4.12 program from Systat Software Inc. After subtraction of the baseline, the peaks were fitted with mixed Gauss-Lorentz functions. The normalized sub-peak areas were then compared in order to obtain information about the changes in surface functional groups after anchoring the metals.

3. Results and discussion

3.1. Configuration of the Ir—La complex

As the carbon support material for the Ir—La/C catalyst is inert, it is not expected to directly influence the catalytic mechanism significantly. This allowed us to model the structure and mechanism for the Ir—La complex in the gas phase, decreasing the computational cost of such studies (Fig. 1). From previous work [11], the composition of the Ir—La/C catalyst was experimentally determined to be $LaIr(CO)_2I_3R$, where R is a negatively charged surface site to which the complex is bound, with the La in its +3 oxidation state and the Ir in either its +1 or +3 oxidation state. La^{3+} cations

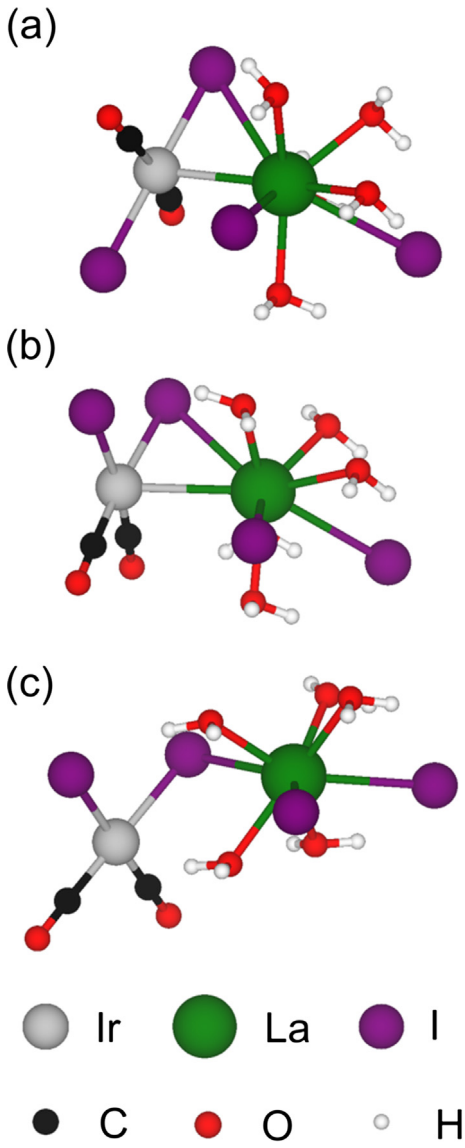

Fig. 1. Optimized configurations for the trans (a), closed cis (b), and open cis (c) configurations of the Ir—La complex with iodine ligands.

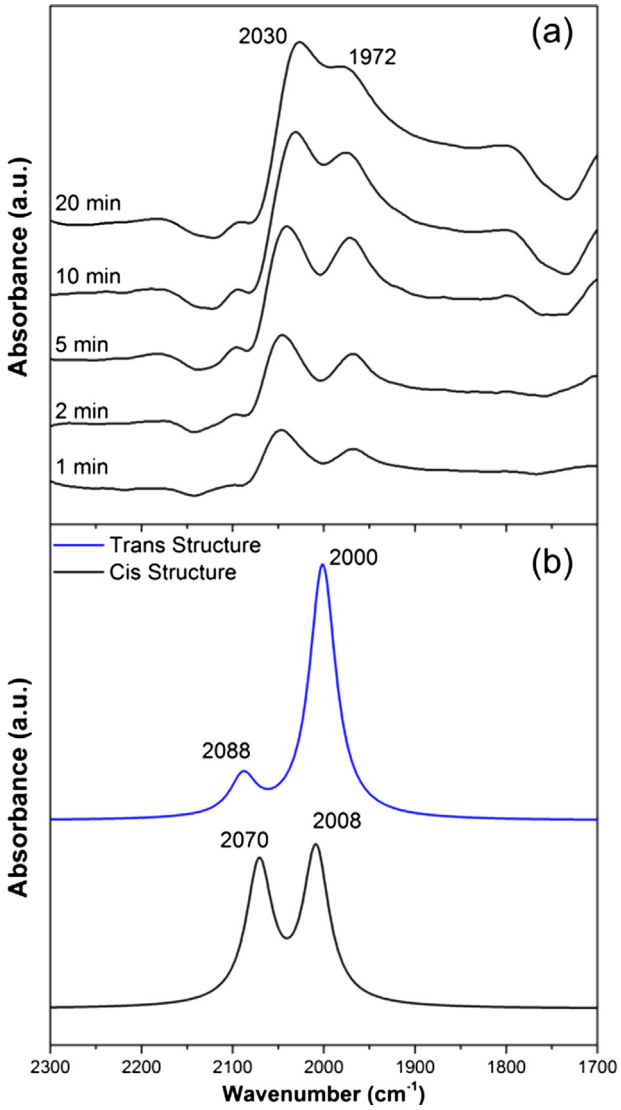

Fig. 2. ATR-FTIR spectra for CO adsorption at 513 K and 1.00 bar over Ir—La/C during syngas pretreatment ($CO:H_2$ = 4:1) (a). DFT calculated IR spectra of the CO stretching modes in the trans and open cis configurations of the Ir—La complex (b). The Ir—La complex had chlorine ligands in both the experimental and theoretical results as the Ir—La/C catalyst measured here has yet to be exposed to MeI (see Fig. S3 for model structures with chlorine ligands).

form a capped trigonal prism coordination environment, with a nine-fold coordination [20,47]. Ir is present in either a six-fold coordinated octahedral complex for Ir^{3+} or a four-fold coordinated square planar complex for Ir^{+} [20,48]. As La forms very weak bonds with CO [11], the two CO molecules are more likely to be bonded to Ir. Furthermore, in its formal +1 oxidation state, the Ir center needs two additional ligands. In order for the Ir complex to be overall charge neutral, at least one of the additional ligands must be either iodine or the surface binding site, R. As the Ir center is likely the active site for the carbonylation reaction based on the similarity to the homogeneous system [16], a setup with La bonded to the surface is more plausible to allow greater access to the Ir center. Since Ir^{+} has to adopt a square planar configuration [20,48], the remaining coordination site could be either a direct Ir—La bond [11] or an iodine bridge between the two metals.

The coordination sphere of the La was modeled with three iodine ligands, one of which is representing the unknown oxidizing surface site R as the anchor point. The remaining sites to reach the nine-fold coordination were filled with water as the simplest neutral ligand present during the synthesis of the catalyst. In the combined Ir—La complex, one water molecule was removed from La to allow for a potential Ir—La bond to form. The resultant Ir—La gas phase complexes are shown in Fig. 1.

A direct metal-metal bond between Ir and La was found to be unstable in the complex from DFT; the Ir and La are therefore bridged by an iodine with three possible configurations (Fig. 1). Two different isomers can be distinguished on behalf of a trans (Fig. 1a) or cis (Fig. 1b/c) configuration of alike ligands on the Ir, with the cis configurations being ~65 kJ/mol more stable than the trans. Of the two cis configurations, the open structure (Fig. 1c) was found to be more favorable by ~5 kJ/mol.

The greater stability of the cis configuration of the Ir—La complex over the trans configuration suggests that the former might be present under catalytic conditions (i.e. a temperature of 513 K and a syngas pressure of 1 bar or higher). This was tested by recording ATR-FTIR spectra during the syngas pretreatment of the initially synthesized Ir—La/C catalyst. As shown in Fig. 2a, two peaks with comparable intensities at 2030 and 1972 cm^{-1} are present and become stable after 20 min of flowing syngas over the Ir—La/C catalyst. It should be noted that the Ir—La/C catalyst has chlorine ligands instead of iodine ligands in the spectra shown in Fig. 2a due to the catalyst synthesis conditions (see Section 2.2). Theoretical IR spectra were generated for both the open cis and trans configurations and the resulting spectra are shown in Fig. 2b. In order to match with experimental conditions, the spectra shown in Fig. 2b are for Ir—La complexes where the iodine ligands were replaced with chlorine (Fig. S3). Both structures result in two peaks at 2070/2088 and 2008/2000 cm^{-1} for the open cis and trans structures, respectively, that correspond to the symmetric and asymmetric CO stretch [18,49,50]. While both structures result in an over prediction of the CO stretch frequencies, the peak separation for the open cis configuration is consistent with the experimental ATR-FTIR spectra, i.e. 58 and 62 cm^{-1} separation between the two modes in the experimental spectra and open cis theoretical spectra, respectively. Therefore, the cis configuration is the most likely structure of the Ir—La complex, which is consistent with the homogeneous Ir and Rh catalysts [17].

While the cis configuration of the Ir—La complex is more likely to be the active site for the Ir—La/C catalyst as compared to the trans configuration, there remains the question of whether or not there is a direct Ir—La bond within the complex in addition to the bridging iodine ligands. As the covalent radii [51] of La and Ir are 2.07 Å and 1.41 Å, respectively, a covalent bond can be formed between these elements for distances less than (2.07 + 1.41) Å = 3.48 Å. Using this distance as a benchmark, it is clear that the closed cis configuration (Fig. 1b) has a stable, direct Ir—La bond, while the open cis configuration (Fig. 1c) has only the bridging iodine. The direct Ir—La bond observed for the closed cis configuration is consistent with high-angle annular dark-field scanning transmission electron microscopy (HAADF STEM) images [11]. However, it is important to note that the HAADF STEM images are taken at room temperature and under vacuum, while the methanol carbonylation reaction is performed at 513 K and a total pressure of 17 bar. The effect of temperature on the stability of the closed cis configuration was examined via an *Ab Initio* Molecular Dynamics (AIMD) simulation at 513 K. After 1.5 ps in the AIMD simulation, the closed cis configuration (Fig. 1b) relaxed to the open cis configuration (Fig. 1c), meaning that the Ir—La bond is broken. As the closed and open cis configurations are similar in terms of their energetic favorability, these results suggest the open cis configuration is the likely structure present under reaction conditions.

3.2. Methanol carbonylation mechanism on the Ir—La complex

The possible roles of the La in the Ir—La/C catalyst include: (1) a surface anchor point for the Ir complex due to La's high affinity to oxygen, (2) a Lewis acid by bridging with the Ir through a CO and thereby assisting in the migratory insertion step, as proposed in the previous study [11], and (3) an iodine acceptor, similar to the promoter effect in the homogeneous catalyst system [15]. Mechanism 2 was determined to be unlikely to occur as the switch in bridging ligand between Ir and La from iodine to CO prior to the CO insertion step was endothermic by ~77 kJ/mol (Fig. S5). The addition of entropy contributions is not expected to change the favorability of mechanism 2 as such factors were found to increase the reaction energies for non-adsorption/desorption reactions on average by 6 kJ/mol (Figs. 4, S4, and S7). It is clear from a comparison of both the DFT and Gibbs reaction energy profiles for mechanisms 1 and 3 that these two mechanisms have similar energetics overall, but mechanism 3 favors the formation of the acetyl species to a greater degree (Figs. 4, S4, and S7). Therefore, this mechanism will be discussed in more detail here (Fig. 3 and Fig. 4), while the details of the other mechanisms are shown in the Supplementary Material.

Starting from the open cis configuration of the Ir—La complex, MeI oxidatively adds to the Ir center forming a 6-fold coordinated Ir^{3+} structure, as shown in Fig. 3B and C. As the structure of the Ir in the initial open cis configuration (Fig. 3A) resembles the homogeneous catalyst, the addition of MeI was studied as a S_N2 reaction with the methyl and iodine adding trans to each other [52]. Four different configurations were tested as possible structures for the $[IrMe(CO)_2I_3]^-$ complex in the Ir—La catalyst (Fig. S6), and configurations B and C in Fig. 3 were found to be the most stable structures. After MeI addition, the La accepts an iodine from the Ir center, allowing a third CO to add onto the Ir center (Fig. 3E). This step is followed by the migratory insertion of CO into the Ir—Me bond and the formation of the acetyl functional group (Fig. 3F). Finally, the acetyl functional group combines with an iodine on the Ir center to form the AcI product, reducing the Ir complex from Ir^{3+} to Ir^+ (Fig. 3G), which then relaxes back into the starting open cis configuration (Fig. 3A).

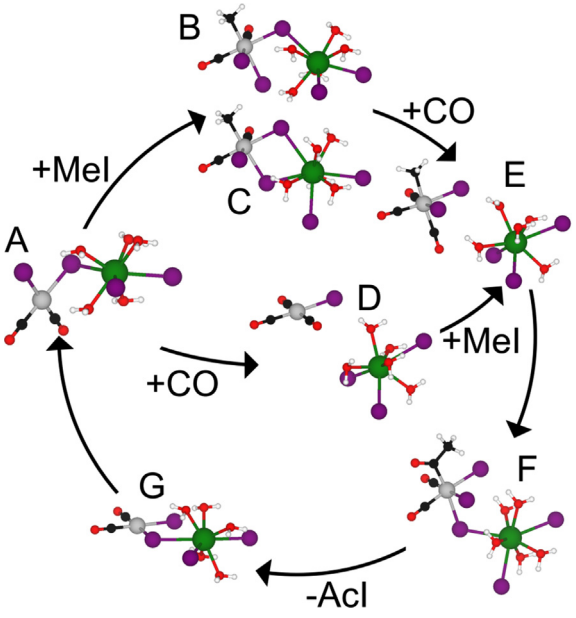

Fig. 3. Reaction scheme for methanol carbonylation on the Ir—La heterogeneous catalyst complex with the La promoter acting as an iodine acceptor (mechanism 3). Sphere colors are identical to those shown in Fig. 1.

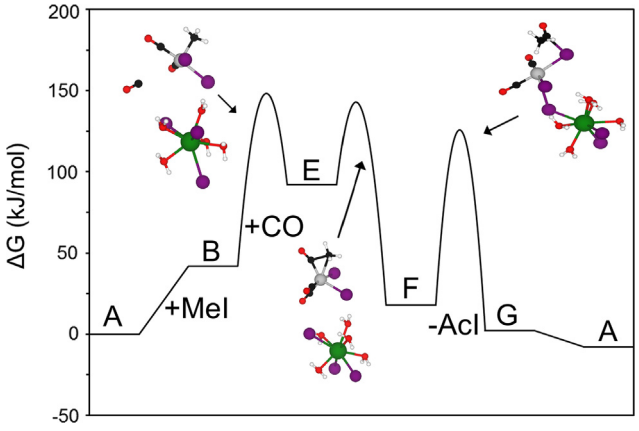

Fig. 4. Gibbs energy profile for methanol carbonylation on the Ir—La heterogeneous catalyst complex with the La promoter acting as an iodine acceptor (mechanism 3). The Gibbs energy was calculated at a temperature of 513 K, a total pressure of 17 bar, a CO concentration of 17.3 mol%, a MeI concentration of 1.8 mol%, and an AcI concentration of 1.8 mol%, consistent with the catalytic experiments performed in our previous work [11], and the scale is relative to the catalyst, MeI, CO, and AcI at infinite separation in the gas phase. The labels (A-G) refer to the configurations shown in Fig. 3 and the shown configurations are the noted transition states where the sphere colors are identical to those shown in Fig. 1. Note, structures C and D from Fig. 3 are not shown as they have the same Gibbs energy as structure B (i.e. structures B, C, and D have Gibbs energies of 42.6, 40.9, and 40.7 kJ/mol, respectively, relative to structure A and either MeI or CO as needed). The DFT reaction energy profile is shown in Fig. S7 and the MEPs for the transition states are shown in Fig. S9.

As methanol carbonylation occurs on the Ir—La/C catalyst under high pressures, a possible variation on mechanism 3 was examined where 3CO molecules add to the Ir^+ structure forming an $[Ir(CO)_3I]$ complex prior to MeI addition (Fig. 3D). In this variation, the La still acts as an iodine acceptor, but the iodine transfer occurs before the addition of MeI to the Ir^+ center. All other reactions occur in a similar manner to that discussed above. The energetics for this mechanism calculated using DFT and Møller-Plesset Perturbation Theory are consistent, as shown in the Supplementary Material (Fig. S7).

The Gibbs energy profile for the mechanism presented in Fig. 3 is shown in Fig. 4. It is clear that the first several steps are endergonic due to the loss of degrees of freedom for the adsorbing MeI and CO species. However, once the $[IrMe(CO)_3I_2]$ species is formed by the abstraction of an iodine from the Ir center by the La center, the remaining reaction steps are exergonic. For this mechanism, we calculated the Gibbs activation barriers for the CO adsorption, CO insertion, and AcI elimination steps. The CO adsorption (Fig. 4B to E) and AcI elimination steps (Fig. 4F to G) have similarly high Gibbs energy barriers of 106 and 107 kJ/mol, respectively, while the CO insertion step (Fig. 4E to F) has a moderate barrier of 51 kJ/mol. In fact, the Gibbs energy profile for this mechanism predicts a possible kinetic trap for the reaction at the $[IrAc(CO)_2I_3]^-$ species, suggesting that this species could be a rate controlling intermediate and therefore potentially measurable under reaction conditions. The CO adsorption step could be a rate controlling reaction step as well (Fig. 4B to E).

We note that for the calculation of the Gibbs activation barriers for CO adsorption and AcI elimination, the adsorbing/desorbing species (i.e. CO and AcI) were treated as if they had lost all of their translational and rotational degrees of motion in the transition state. While the translational and rotational contributions are likely reduced relative to the gas phase molecule, the adsorbing CO and desorbing AcI will likely retain some of their translational and rotational modes of motion in their respective transition states. Therefore, this assumed loss of translational and rotational degrees of motion in the activated adsorption/desorption

pathways' transition states likely results in an over prediction of the calculated Gibbs activation barrier for such reactions and should be taken as an upper bound for the actual activation barrier.

The greater favorability of the mechanism with the La promoter acting as an iodine acceptor (Figs. 3 and 4) over the other tested mechanisms is consistent with the homogeneous-promoted Ir catalyst, as the addition of a Ru promoter was found to assist in the abstraction of an iodine from the Ir center, allowing 3CO to adsorb onto the Ir [15,17]. Theoretical calculations for the homogeneous system found that the Ir complex with 3CO adsorbed had a substantially lower activation barrier (by 35 to 47 kJ/mol) for CO insertion than that of the Ir complex with 2CO [15]. By calculating the CO insertion barrier for mechanism 1 (Fig. S8), we can now make a similar comparison for the heterogeneous Ir—La/C catalyst and we find that when the La acts as an iodine abstractor, similar to the homogeneous Ru promoter, the Gibbs activation barrier for CO insertion is ~47 kJ/mol lower. These theoretical results suggest that the heterogeneous Ir and La complexes interact in a similar manner to the homogeneous-promoted Ir catalyst.

The potential weakness of this mechanism is that two of the structures, Fig. 3D and E, have the Ir and La connected only via hydrogen bonds between the ligands. Using the van der Waals corrected optB88-vdW functional [53,54], we estimated the bond strength between the Ir and La complexes in these two structures to be 20–30 kJ/mol (see Fig. S11 for details). As such, the structures could fully separate if the subsequent migratory insertion reaction does not occur fast enough. However, the moderate Gibbs activation barrier and large exergonic reaction energy of ~−74 kJ/mol during migratory insertion (Fig. 4E to F) suggests that the formation of the acetyl complex occurs rapidly and prevents the separation of Ir and La, indicating that this mechanism is reasonable.

The validity of the mechanism for MeI carbonylation proposed above in Fig. 3 was probed experimentally using *in situ* ATR-FTIR spectroscopy and DFT generated IR spectra (see Table S1 for the calculated C-O vibrational frequency values). As shown in Fig. 5a, the Ir—La/C catalyst was first pretreated with syngas after calcination with N_2 for 20 min, leading to the formation of two main peaks at 2030 and 1972 cm^{-1}, which is consistent with the symmetric and asymmetric CO stretching modes shown in Fig. 2 [18,49,50]. In addition to these CO stretching peaks, a small peak appears at around 2085 cm^{-1} which aligns with both the vibration of CO adsorbed on the carbon support and the CO stretch in the $[Ir(CO)_3I]$ structure (Fig. 5b configuration D). Additionally, the peak at 1685 cm^{-1} was attributed to the formation of the C=O bond in carboxylate or carbonate on the carbon support [50,55]. After 20 min of syngas pretreatment, methanol and syngas were introduced and no noticeable changes in the spectra were observed, suggesting that methanol is not directly carbonylated by CO over the Ir—La/C catalyst (Fig. S12).

The introduction of MeI and syngas to the Ir—La/C catalyst led to the formation of a new peak at 1711 cm^{-1} (Fig. 5a). This peak is consistent with the theoretically predicted acetyl C=O vibrational mode on the $[IrAc(CO)_2I_3]^-$ complex (Fig. 5b configuration F), and the $[IrAc(CO)_2I_3]^-$ and $[RhAc(CO)I_3]^-$ complexes in the analogous homogeneous Ir and Rh catalysts, respectively [15,56–58]. Additionally, the 1711 cm^{-1} peak measured here is redshifted from the gas phase acetyl stretch in AcI by ~100 cm^{-1} suggesting the acetyl species is strongly interacting with the catalyst, which is unlikely to occur with the activated carbon surface [59,60]. The accumulation of the $[IrAc(CO)_2I_3]^-$ complex (Fig. 3F) suggests that this complex is a rate controlling intermediate over the Ir—La/C catalyst, which is consistent with the DFT-predicted kinetic trap at the $[IrAc(CO)_2I_3]^-$ species in Fig. 4. When a similar experiment is performed with N_2 as the carrier gas instead of syngas (Fig. S14), it is clear that the 1711 cm^{-1} peak quickly forms and then disappears upon exposure of the Ir—La/C catalyst to MeI.

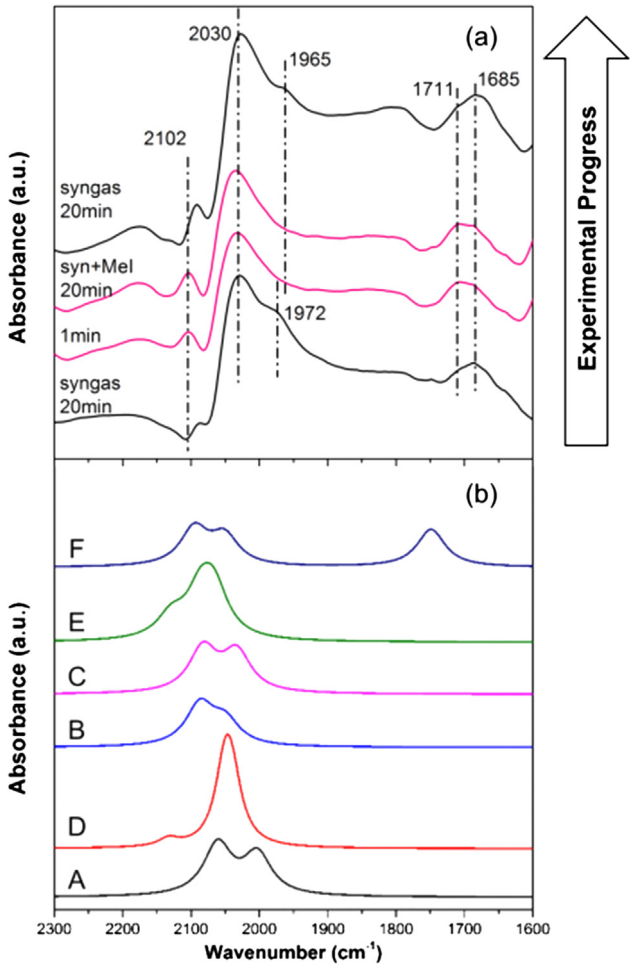

Fig. 5. (a) ATR-FTIR spectra obtained by flowing different reactants over the Ir—La/C catalyst at 513 K and 1.00 bar of syngas for the bottom spectrum and 3.75 bar of syngas for the other spectra (syngas CO:H_2 ratios were 4:1). The spectra were taken in the order from the bottom to the top. (b) DFT calculated IR spectra of the CO stretching modes for the stable intermediate Ir—La complex configurations during the carbonylation of methanol. The labels (A–F) refer to the configurations shown in Fig. 3, and the normal modes are visualized in Fig. S13.

These experiments support the assignment of the 1711 cm^{-1} peak to the formation of the acetyl functional group on the Ir^{3+} complex.

The final change in the ATR-FTIR spectra upon the exposure of MeI to the Ir—La/C catalyst is the disappearance of the 1972 cm^{-1} peak (Fig. 5a). Based on the DFT-calculated vibrational frequencies for the $[IrMe(CO)_2I_3]^-$, $[IrMe(CO)_3I_2]$, and $[IrAc(CO)_2I_3]^-$ configurations (Fig. 3 B/C, E, and F, respectively), the oxidative addition of MeI to the Ir—La complex results in an average blue shift in the symmetric and asymmetric CO stretch frequencies by ~27 and 47 cm^{-1}, respectively, relative to the $[Ir(CO)_2I_2]^-$ configuration. The ~1.8 times greater blue shift in the asymmetric CO stretch peak compared to the symmetric CO stretch peak places the two peaks closer in proximity to each other. This suggests that the disappearance in the 1972 cm^{-1} peak observed experimentally is caused by an overlap between the two CO stretch peaks. The fast disappearance of the 1972 cm^{-1} peak in the experimental spectra after 1 min indicates that the oxidative addition of MeI is fast, which is consistent with the promoted homogeneous system [21].

The role of La in this catalytic reaction was further investigated by measuring the IR spectra using an identical procedure for an Ir/C catalyst with an equivalent amount of Ir (Fig. S15). The spectra comparisons showed that the dominant structures on the Ir/C and Ir—La/C catalysts after the introduction of MeI are the

$[IrMe(CO)_3I_2]$ and $[IrAc(CO)_2I_3]^-$ configurations, respectively. These results confirm the theoretical prediction in Fig. 4 that the La promoter accelerates the CO insertion step (Fig. 3E to F), consistent with the behavior of the promoted homogenous catalyst [15].

Overall, through the use of DFT and ATR-FTIR, the MeI carbonylation mechanism for the Ir—La/C heterogeneous catalyst was determined to be similar to that of the promoted homogeneous catalyst – with La acting as an iodine acceptor to accelerate CO insertion. Furthermore, the $[IrAc(CO)_2I_3]^-$ species was found to be a rate controlling intermediate over the Ir—La/C heterogeneous catalyst.

3.3. Surface binding site for the Ir—La complex

Since the activity and mechanism for carbonylation over the Ir—La/C catalyst relies on the isolation of the Ir—La complex on the activated carbon support, identifying the immobilization site for the complex is a key factor in the further design of such single-site heterogeneous catalysts [11]. As a computational model for the interaction between the complex and the carbon surface, the catalyst in the open cis configuration was adsorbed on pristine graphene (Fig. 6a). The structure of the Ir—La complex remains unchanged during the adsorption and the large distance of approximately 5.31 Å between La and the surface indicates there are no interactions between them. This is consistent with the weak binding energy of only −16.2 kJ/mol. Thus, this structure cannot explain the long-term stability of the catalyst observed in the experiment [11] and the basal plane of the carbon support is therefore not the main adsorption site.

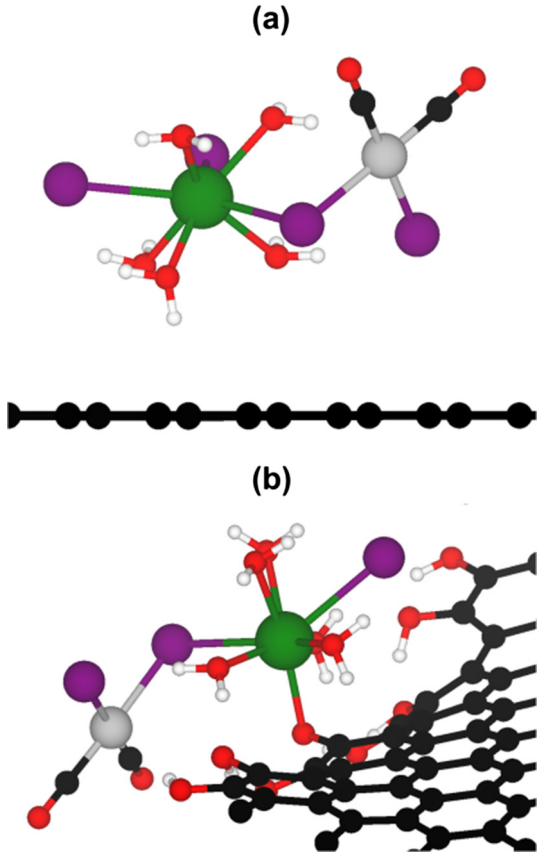

Fig. 6. Adsorption of the open cis configuration of the catalyst on the (a) pristine graphene surface and (b) AGNR-OH surface. Due to the formation of hydrogen bridges between the terminating hydroxy groups, the edge of the AGNR-OH is corrugated. Sphere colors are identical to those shown in Fig. 1.

Various oxidizing surface sites, e.g. defects [36,61], edges, or adatoms like oxygen [62], can be found on the activated carbon surface, which can act as potential binding sites for the Ir—La complex. With La showing an affinity to oxygen, the adsorption of the Ir—La complex on OH-passivated armchair-graphene nanoribon (AGNR-OH) was investigated in order to simulate the oxidized edge sites likely present on the activated carbon support. The optimized structure for the open cis Ir—La complex adsorbed on the AGNR-OH surface is shown in Fig. 6b. Due to the formation of a chemical bond between La and the surface oxygen on the AGNR-OH surface, the binding energy of −227.94 kJ/mol for the Ir—La complex on AGNR-OH is much larger than on pristine graphene. Additionally, the strong interaction with the surface is apparent as the La-O distance is only 2.48 Å between the surface oxygen and La as opposed to the 2.54–2.65 Å La—O distance between the water ligands and La. Therefore, the Ir—La complex is expected to attach to the carbon support through the surface oxygen species bound to the La.

The attachment of the Ir—La complex to the carbon support through an oxygen functional group was confirmed using ATR-FTIR. The addition of the Ir—La complex to the activated carbon support only affects the peaks in the C—O bond adsorption region from 1000 to 1300 cm^{-1} (Fig. S17). As shown in Fig. 7a, the apex of the C—O band shifts from 1244 cm^{-1} to 1210 cm^{-1}, implying that the C—O bond is involved in anchoring the Ir—La complex as predicted from DFT. Based on a deconvolution of this region (Fig. 7b), we propose that the Ir—La complex is bound to the carbon support via a broken C—O—C ether bond (assigned based on the peaks at 1244 and 1143 cm^{-1}) [63], which is corroborated by the emergence of a new broad band at 1068 cm^{-1} due to the adsorption of the Ir—La complex and formation of a C—O—La bond.

3.4. Promoter effect

From our mechanistic studies, we have determined that the most likely carbonylation mechanism over the Ir—La/C catalyst involves the La promoting CO insertion by abstracting an iodine from the active Ir center (Fig. 3). This mechanism differs significantly from that proposed previously on Ir—La/C [11], where La acts as a Lewis acid by bonding to the Ir center via a CO ligand (Fig. S5). This assertion was based on: (1) the most common bonding method of lanthanides and transition metal carbonyls (i.e. Ln–OC–M, where Ln = lanthanide, M = transition metal) [64,65] and (2) the linear relationship between the activity of an Ir-X/C catalyst and the electronegativity of X (where X = promoter metal) [11]. Our DFT results show that the formation of the La–OC–Ir complex is unlikely due to the endothermic formation energy of ~77 kJ/mol (Fig. S5) and lack of agreement between the ATR-FTIR and DFT generated IR spectra for the stable intermediates in this mechanism (Fig. S10).

While we have ruled out the possibility of the La and Ir bridging within the Ir—La/C catalyst via a CO ligand, the effect of the second metal's (i.e. La) electronegativity and iodine affinity relative to the Ir center is likely to be a crucial factor in the promotional effect of the second metal. For the fast insertion of CO into the Ir-methyl bond, one of the iodine ligands must be abstracted from the Ir center (Fig. 3). Considering this effect alone, we would expect that an effective promoter metal would be one that had a lower electronegativity and higher iodine affinity than Ir in order to draw an iodine ligand away from the Ir center. Additionally, the transfer of the iodine ligand from the Ir center results in an increase in the formal charge on the overall Ir complex from −1 to 0. This suggests that in abstracting the iodine ligand from the Ir complex, the La complex has pulled charge from the Ir complex and is therefore acting as a Lewis acid, which is consistent with the previous work [11].

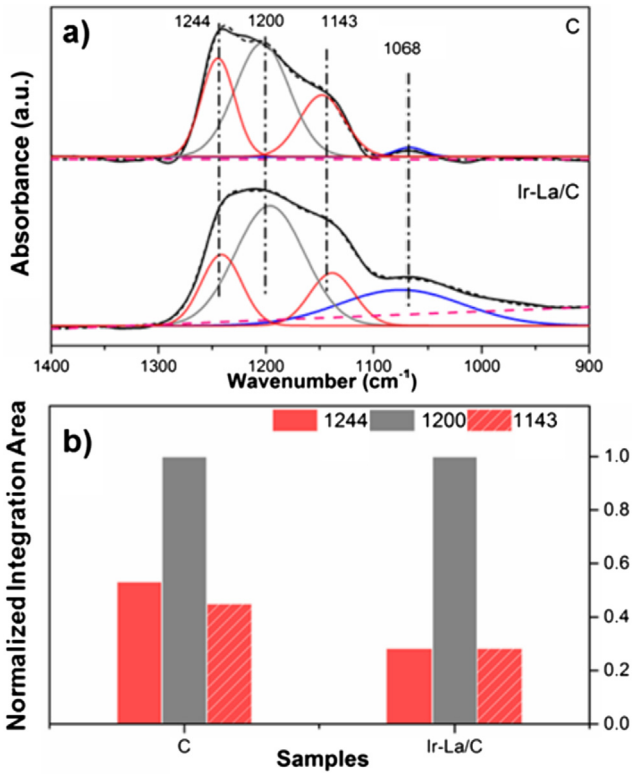

Fig. 7. ATR-FTIR spectra and their deconvolution for pure activated carbon (C) and Ir—La/C catalyst after syngas pretreatment ($CO:H_2$ = 4:1) at 513 K and 1 bar (a). The area of each deconvoluted peak from panel (a) are normalized to the area of the 1200 cm^{-1} peak (b). Here, the 1244 and 1143 cm^{-1} peaks were assigned to the symmetric and asymmetric vibrations of C—O—C ether bonds, respectively,[63] while the 1200 cm^{-1} peak was assigned to the surface C—H bending vibration and C—O vibration in ester species [50,55]. Since the C=O absorption peak remained unchanged, the ester and its C—O absorption peak should be stable, and considering the instability of a direct metal-carbon bond (Fig. 6a) it is unlikely that the C—H bond is broken by Ir—La to replace the H atom. Therefore, we speculate that the 1200 cm^{-1} peak would not change and that said peak could be used as an area benchmark, as done in panel (b).

One additional effect to consider is the dispersion of the Ir—La complex on the support. As the mechanism determined here for the heterogeneous Ir—La/C catalyst is similar to that of the homogeneous-promoted Ir catalyst, it stands to reason that isolated Ir atom sites are required in the heterogeneous catalyst. Due to the high affinity of La for oxygen, the La was found to be the surface attachment site for the Ir—La complex (Fig. 6). This suggests that the oxygen affinity of the promoter can be used to obtain greater dispersion of Ir atoms on the support and thus is a significant factor in the performance of a promoted Ir heterogeneous catalyst.

4. Conclusions

In summary, using a combination of DFT and ATR-FTIR, we have determined the structure and the corresponding methanol carbonylation mechanism for a single-site heterogeneous Ir—La/C catalyst. Based on our results, we propose that the promoter effect of La in this system is two-fold: (1) atomically dispersing the Ir centers on the activated carbon support and (2) acting as a Lewis acid relative to the Ir center and abstracting an iodine from the Ir, thereby accelerating the CO insertion step. The similarities between the mechanism and promoter effect for the heterogeneous Ir—La/C catalyst to the homogeneous-promoted Ir catalyst, i.e. the accelerated insertion of CO via the abstraction of an iodine ligand, shows that this heterogeneous system provides a bridge between the two paradigms. Overall, this work provides insight into the atomistic-level structure and behavior of the single-site Ir—La/C catalyst that can be used to further design and optimize heterogeneous catalysts for the carbonylation of methanol.

Acknowledgements

J.S.M and A.J.R.H. were supported by the National Science Foundation CAREER program under contract number CBET-1653561. J.S.M. and A.J.R.H. also acknowledge funding from the National Science Foundation EAGER program under contract number CBET-1552320, as well as institutional funds from the Gene and Linda Voiland School of Chemical Engineering and Bioengineering. J.S.M. thanks the donors of the American Chemical Society Petroleum Research Fund. J.Z., X.P.H., and Y.W. were supported by the U.S. Department of Energy grant DE-FG02-05ER15712. I.V. thanks the Research Internships in Science and Engineering program, which is supported by the Federal Republic of Germany through the Federal Ministry of Education and Research. The Pacific Northwest National Laboratory is operated by Battelle for the U. S. DOE. The authors thank Greg Collinge for his helpful comments and discussions.

Appendix A. Supplementary material

Supplementary data associated with this article can be found, in the online version, at https://doi.org/10.1016/j.ejpb.2018.02.018.

References

[1] Z.-T. Wang, M.T. Darby, A.J. Therrien, M. El-Soda, A. Michaelides, M. Stamatakis, E.C.H. Sykes, Preparation, structure, and surface chemistry of Ni–Au single atom alloys, J. Phys. Chem. C 120 (2016) 13574–13580.
[2] F.R. Lucci, M.T. Darby, M.F. Mattera, C.J. Ivimey, A.J. Therrien, A. Michaelides, M. Stamatakis, E.C. Sykes, Controlling hydrogen activation, spillover, and desorption with Pd-Au single-atom alloys, J. Phys. Chem. Lett. 7 (2016) 480–485.
[3] P. Serna, B.C. Gates, Molecular metal catalysts on supports: organometallic chemistry meets surface science, Acc. Chem. Res. 47 (2014) 2612–2620.
[4] J.D. Kistler, N. Chotigkrai, P. Xu, B. Enderle, P. Praserthdam, C.Y. Chen, N.D. Browning, B.C. Gates, A single-site platinum CO oxidation catalyst in zeolite KLTL: microscopic and spectroscopic determination of the locations of the platinum atoms, Angew. Chem. Int. Ed. 53 (2014) 8904–8907.
[5] J.O. Ehresmann, P.W. Kletnieks, A. Liang, V.A. Bhirud, O.P. Bagatchenko, E.J. Lee, M. Klaric, B.C. Gates, J.F. Haw, Evidence from NMR and EXAFS studies of a dynamically uniform mononuclear single-site zeolite-supported rhodium catalyst, Angew. Chem. Int. Ed. 45 (2006) 574–576.
[6] N. Nikbin, N. Austin, D.G. Vlachos, M. Stamatakis, G. Mpourmpakis, Catalysis at the sub-nanoscale: complex CO oxidation chemistry on a few Au atoms, Catal. Sci. Technol. 5 (2015) 134–141.
[7] G. Liu, A.W. Robertson, M.M.-J. Li, W.C.H. Kuo, M.T. Darby, M.H. Muhieddine, Y.-C. Lin, K. Suenaga, M. Stamatakis, J.H. Warner, S.C.E. Tsang, MoS_2 monolayer catalyst doped with isolated Co atoms for the hydrodeoxygenation reaction, Nat. Chem. (2017), https://doi.org/10.1038/nchem.2740.
[8] Y.G. Wang, D. Mei, V.A. Glezakou, J. Li, R. Rousseau, Dynamic formation of single-atom catalytic active sites on ceria-supported gold canoparticles, Nat. Commun. 6 (2015) 6511.
[9] B. Qiao, A. Wang, X. Yang, L.F. Allard, Z. Jiang, Y. Cui, J. Liu, J. Li, T. Zhang, Single-atom catalysis of CO oxidation using Pt_1/FeO_x, Nat. Chem. 3 (2011) 634–641.
[10] C. Thomas, G. Süss-Fink, Ligand effects in the rhodium-catalyzed carbonylation of methanol, Coord. Chem. Rev. 243 (2003) 125–142.
[11] J.H. Kwak, R. Dagle, G.C. Tustin, J.R. Zoeller, L.F. Allard, Y. Wang, Molecular active sites in heterogeneous Ir-La/C-catalyzed carbonylation of methanol to acetates, J. Phys. Chem. Lett. 5 (2014) 566–572.
[12] C. Copéret, M. Chabanas, R.P. Saint-Arroman, J.-M. Basset, Homogeneous and heterogeneous catalysis: bridging the gap through surface organometallic chemistry, Angew. Chem. Int. Ed. 42 (2003) 156–181.
[13] F.E. Paulik, J.F. Roth, Novel catalysts for the low-pressure carbonylation of methanol to acetic acid, Chem. Commun. (1968) 1578.
[14] D. Forster, T.C. Singleton, Homogeneous catalytic reactions of methanol with carbon monoxide, J. Molec. Catal. 17 (1982) 299–314.
[15] A. Haynes, P.M. Maitlis, G.E. Morris, G.J. Sunley, H. Adams, P.W. Badger, C.M. Bowers, D.B. Cook, P.I.P. Elliott, T. Ghaffar, H. Green, T.R. Griffin, M. Payne, J.M. Pearson, M.J. Taylor, P.W. Vickers, R.J. Watt, Promotion of iridium-catalyzed methanol carbonylation: mechanistic studies of the Cativa process, J. Am. Chem. Soc. 126 (2004) 2847–2861.

[16] P.M. Maitlis, A. Haynes, G.J. Sunley, M.J. Howard, Methanol carbonylation revisited: thirty years on, J. Chem. Soc., Dalton Trans. (1996) 2187–2196.
[17] A. Haynes, Chapter 1 – catalytic methanol carbonylation, Adv. Catal. 53 (2010) 1–45.
[18] D. Forster, Kinetic and spectroscopic studies of the carbonylation of methanol with an iodide-promoted iridium catalyst, J. Chem. Soc., Dalton Trans. (1979) 1639–1645.
[19] A. Jess, P. Wasserscheid, Chemical Technology, Wiley VCH Verlag, Weinheim, 2013.
[20] F. Cotton, G. Wilkinson, C. Murillo, M. Bochmann, Advanced Inorganic Chemistry, sixth ed., Wiley VCH Verlag, Weinheim, 1999.
[21] G.J. Sunley, D.J. Watson, High productivity methanol carbonylation catalysis using iridium: the Cativa™ process for the manufacture of acetic acid, Catal. Today 58 (2000) 293–307.
[22] G. Kresse, J. Hafner, *Ab Initio* molecular dynamics for liquid metals, Phys. Rev. B 47 (1993) 558–561.
[23] G. Kresse, J. Furthmüller, Efficiency of *ab-initio* total energy calculations for metals and semiconductors using a plane-wave basis set, Comput. Mater. Sci. 6 (1996) 15–50.
[24] G. Kresse, J. Furthmüller, Efficient iterative schemes for *ab initio* total-energy calculations using a plane-wave basis set, Phys. Rev. B 54 (1996) 11169–11186.
[25] G. Kresse, D. Joubert, From ultrasoft pseudopotentials to the projector augmented-wave method, Phys. Rev. B 59 (1999) 1758–1775.
[26] P.E. Blöchl, Projector augmented-wave method, Phys. Rev. B 50 (1994) 17953–17979.
[27] J.P. Perdew, K. Burke, M. Ernzerhof, Generalized gradient approximation made simple, Phys. Rev. Lett. 77 (1996) 3865–3868.
[28] E.D. Stevens, J. Rys, P. Coppens, Quantitative comparison of theoretical calculations with the experimentally determined electron density distribution of formamide, J. Am. Chem. Soc. 100 (1978) 2324–2328.
[29] G. Henkelman, B.P. Uberuaga, H. Jónsson, A climbing image nudged elastic band method for finding saddle points and minimum energy paths, J. Chem. Phys. 113 (2000) 9901–9904.
[30] D. Sheppard, R. Terrell, G. Henkelman, Optimization methods for finding minimum energy paths, J. Chem. Phys. 128 (2008) 134106.
[31] E. Bitzek, P. Koskinen, F. Gahler, M. Moseler, P. Gumbsch, Structural relaxation made simple, Phys. Rev. Lett. 97 (2006) 170201.
[32] S.A. Trygubenko, D.J. Wales, A doubly nudged elastic band method for finding transition states, J. Chem. Phys. 120 (2004) 2082–2094.
[33] G. Collinge, N. Kruse, J.-S. McEwen, Role of carbon monoxide in catalyst reconstruction for CO hydrogenation: first-principles study of the composition, structure, and stability of Cu/Co(10–12) as a function of CO pressure, J. Phys. Chem. C 121 (2017) 2181–2191.
[34] D.A. McQuarrie, Statistical Thermodynamics, first ed., Harper Collins, 1973.
[35] J.-P. Jalkanen, M. Halonen, D. Fernández-Torre, K. Laasonen, L. Halonen, A computational study of the adsorption of small Ag and Au nanoclusters on graphite, J. Phys. Chem. A 111 (2007) 12317–12326.
[36] F. Mehmood, R. Pachter, W. Lu, J.J. Boeckl, Adsorption and diffusion of oxygen on single-layer graphene with topological defects, J. Phys. Chem. C 117 (2013) 10366–10374.
[37] A. Pulido, M. Boronat, A. Corma, Theoretical investigation of gold clusters supported on graphene sheets, New J. Chem. 35 (2011) 2153–2161.
[38] H.J. Monkhorst, J.D. Pack, Special points for brillouin-zone integrations, Phys. Rev. B 13 (1976) 5188–5192.
[39] M. Gajdoš, K. Hummer, G. Kresse, J. Furthmüller, F. Bechstedt, Linear optical properties in the projector-augmented wave methodology, Phys. Rev. B 73 (2006) 045112.
[40] D. Karhánek, T. Bucko, J. Hafner, A density functional theory Study of the adsorption of methane-thiol on the (111) surfaces of the Ni-group metals: II. Vibrational spectroscopy, J. Phys.: Condens. Matter 22 (2010) 265006.
[41] D. Karhánek, Downloads / Utilities / Scripts – David Karhánek, Mar. 27, 2017, <http://homepage.univie.ac.at/david.karhanek/downloads.html>.
[42] D.J. Darensbourg, J.H. Reibenspies, C.-H. Lai, W.-Z. Lee, M.Y. Darensbourg, Analysis of an organometallic iron site model for the heterodimetallic unit of [NiFe]Hydrogenase, J. Am. Chem. Soc. 119 (1997) 7903–7904.
[43] C.-H. Lai, W.-Z. Lee, M.L. Miller, J.H. Reibenspies, D.J. Darensbourg, M.Y. Darensbourg, Responses of the $Fe(CN)_2(CO)$ unit to electronic changes as related to its role in [NiFe]Hydrogenase, J. Am. Chem. Soc. 120 (1998) 10103–10114.
[44] Z.-P. Liu, P. Hu, A density functional theory study on the active center of Fe-only hydrogenase: characterization and electronic structure of the redox states, J. Am. Chem. Soc. 124 (2002) 5175–5182.
[45] Z. Wei, A. Karim, Y. Li, D. King, Y. Wang, Elucidation of the roles of Re in steam reforming of glycerol over Pt–Re/C catalysts, J. Catal. 322 (2015) 49–59.
[46] B.L. Mojet, S.D. Ebbesen, L. Lefferts, Light at the interface: the potential of attenuated total reflection infrared spectroscopy for understanding heterogeneous catalysis in water, Chem. Soc. Rev. 39 (2010) 4643–4655.
[47] S. Cotton, Coordination Chemistry of the Lanthanides, John Wiley & Sons Ltd, New York, 2006.
[48] R.S. Dickson, Organometallic Chemistry of Rhodium and Iridium, Academic Press, London, 1983.
[49] P.I. Elliott, S. Haak, A.J. Meijer, G.J. Sunley, A. Haynes, Reactivity of Ir(III) carbonyl complexes with water: alternative by-product formation pathways in catalytic methanol carbonylation, Dalton Trans. 42 (2013) 16538–16546.
[50] A. Barroso-Bogeat, M. Alexandre-Franco, C. Fernández-González, V. Gómez-Serrano, FT-IR analysis of pyrone and chromene structures in activated carbon, Energy Fuels 28 (2014) 4096–4103.
[51] B. Cordero, V. Gómez, A. Platero-Prats, M. Revés, J. Echeverría, E. Cremades, F. Barragán, S. Alvarez, Covalent radii revisited, Dalton Trans. 2832–2838 (2008).
[52] M. Cheong, T. Ziegler, Density functional study of the oxidative addition step in the carbonylation of methanol catalyzed by $[M(CO)_2I_2]^-$ M = Rh, Ir, Organometallics 24 (2005) 3053–3058.
[53] J. Klimeš, D.R. Bowler, A. Michaelides, Chemical accuracy for the van der Waals density functional, J. Phys.: Condens. Matter 22 (2010) 022201.
[54] J. Klimeš, D.R. Bowler, A. Michaelides, Van der Waals density functionals applied to solids, Phys. Rev. B 83 (2011) 195131.
[55] A. Dandekar, R.T.K. Baker, M.A. Vannice, Characterization of activated carbon, graphitized carbon fibers and synthetic diamond powder using TPD and DRIFTS, Carbon 36 (1998) 1821–1831.
[56] A. Haynes, B.E. Mann, D.J. Gulliver, G.E. Morris, P.M. Maitlis, Direct observation of $MeRh(CO)_2I_3^-$: the key intermediate in rhodium-catalyzed methanol carbonylation, J. Am. Chem. Soc. 113 (1991) 8567–8569.
[57] A. Haynes, B.E. Mann, G.E. Morris, P.M. Maitlis, Mechanistic studies on rhodium-catalyzed carbonylation reactions: spectroscopic detection and reactivity of a key intermediate, $[MeRh(CO)_2I_3]^-$, J. Am. Chem. Soc. 115 (1993) 4093–4100.
[58] D. Forster, On the mechanism of a rhodium-complex-catalyzed carbonylation of methanol to acetic acid, J. Am. Chem. Soc. 98 (1976) 846–848.
[59] J.A. Ramsey, J.A. Ladd, The infrared spectra and vibrational assignments of the acetyl halides, J. Chem. Soc. B (1968) 118–122.
[60] P. Lazar, F. Karlicky, P. Jurecka, M. Kocman, E. Otyepkova, K. Safarova, M. Otyepka, Adsorption of small organic molecules on graphene, J. Am. Chem. Soc. 135 (2013) 6372–6377.
[61] P. Denis, F. Iribarne, Comparative study of defect reactivity in graphene, J. Phys. Chem. C 117 (2013) 19048–19055.
[62] J. Carlsson, F. Hanke, S. Linie, M. Scheffler, Two-step mechanism for low-temperature oxidation of vacancies in graphene, Phys. Rev. Lett. 102 (2009) 166104.
[63] E. Fuente, J.A. Menéndez, M.A. Díez, D. Suárez, M.A. Montes-Morán, Infrared spectroscopy of carbon materials: a quantum chemical study of model compounds, J. Phys. Chem. B 107 (2003) 6350–6359.
[64] A.E. Crease, P. Legzdins, The lewis acidity of organolanthanides. The interaction of cyclopenta-dienyl-lanthanides with some carbonyl and nitrosyl complexes, J. Chem. Soc., Dalton Trans. (1973) 1501–1507.
[65] C.E. Plecnik, S. Liu, J. Liu, X. Chen, E.A. Meyers, S.G. Shore, Lanthanide-transition-metal carbonyl complexes. 1. Syntheses and structures of Ytterbium (II) solvent-separated ion pairs and isocarbonyl polymeric arrays of tetracarbonylcobaltate, Inorg. Chem. 41 (2002) 4936–4943.